

***Design and development of novel biocompatible nanomaterials
for multifunctional applications.***



Thesis submitted in partial fulfillment

for the Award of Degree

Doctor of Philosophy

by

SHIVESH SABBARWAL

**DEPARTMENT OF CHEMICAL
ENGINEERING AND TECHNOLOGY
INDIAN INSTITUTE OF TECHNOLOGY
(BANARAS HINDU UNIVERSITY)
VARANASI – 221 005**

Roll number: 16041007

Year of submission: 2023

Dedicated

to

My Beloved Grandmother,

Dr. Savitri Sabbarwal,

and

My Father,

Satish Kumar Sabbarwal

CERTIFICATE

It is certified that the work contained in the thesis titled '**Design and development of novel biocompatible nanomaterials for multifunctional applications**' by **Shivesh Sabbarwal** has been carried out under my supervision and that this work has not been submitted elsewhere for a degree.

It is further certified that the student has fulfilled all the requirements of Comprehensive Examination, Candidacy and SOTA for the award of Ph.D. Degree.



Dr. Manoj Kumar

(Supervisor)

Department of Chemical Engineering and Technology
Indian Institute of Technology
(Banaras Hindu University)
Varanasi- 221005, India

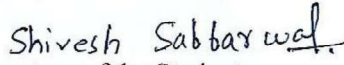
Associate Professor
रासायनिक अभियांत्रिकी एवं प्रौद्योगिकी विभाग
Deptt. of Chemical Engg. & Tech.
भारतीय प्रौद्योगिकी संस्थान
Indian Institute of Technology
काशी हिन्दू विश्वविद्यालय
Banaras Hindu University
वा.रा.प.स./Varanasi-221005

DECLARATION BY THE CANDIDATE

I, Shivesh Sabbarwal, certify that the work embodied in this thesis is my own bona fide work and carried out by me under the supervision of Dr. Manoj Kumar from July 2016 to June 2023, at the Department of Chemical Engineering & Technology, Indian Institute of Technology (Banaras Hindu University), Varanasi. The matter embodied in this thesis has not been submitted for the award of any other degree/diploma. I declare that I have faithfully acknowledged and given credits to the research workers wherever their works have been cited in my work in this thesis. I further declare that I have not willfully copied any other's work, paragraphs, text, data, results, etc., reported in journals, books, magazines, reports dissertations, theses, etc., or available at websites and have not included them in this thesis and have not cited as my own work.

Date: 28-06-2023

Place: IIT (BHU), Varanasi


Signature of the Student

Shivesh Sabbarwal

CERTIFICATE BY THE SUPERVISOR(S)

It is certified that the above statement made by the student is correct to the best of my/our knowledge.



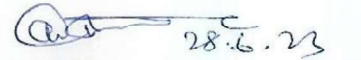
Dr. Manoj Kumar
(Supervisor)

Department of Chemical Engineering and
Technology Indian Institute of Technology
(Banaras Hindu University), Varanasi,
221005, India

सह प्राचार्य

Associate Professor

रासायनिक अभियांत्रिकी एवं प्रौद्योगिकी विभाग
Deptt. of Chemical Engg. & Tech.

 28.6.23

विभागाध्यक्ष/Head
रासायनिक अभियांत्रिकी एवं प्रौद्योगिकी विभाग
Deptt. of Chemical Engg. & Tech
Head of the Department
रासायनिक अभियांत्रिकी एवं प्रौद्योगिकी विभाग
भारतीय प्रौद्योगिकी संस्थान (बनारस हिन्दू विश्वविद्यालय)
Varanasi-221005

Department of Chemical Engineering &
Technology, Indian Institute of Technology
(Banaras Hindu University), Varanasi,
211005, India

COPYRIGHT TRANSFER CERTIFICATE

Title of the Thesis: **Design and development of novel biocompatible nanomaterials for multifunctional applications.**

Name of the Student: **Shivesh Sabbarwal**

Copyright Transfer

The undersigned hereby assigns to the Institute of Technology (Banaras Hindu University) Varanasi all rights under copyright that may exist in and for the above thesis submitted for the award of the Doctor of Philosophy degree.

Date: 28.06.2023

Place: IIT (BHU), Varanasi

Shivesh Sabbarwal
(Shivesh Sabbarwal)

ACKNOWLEDGEMENT

I am deeply grateful to my Supervisor, **Dr. Manoj Kumar**, Associate professor, Department of chemical engineering & Technology, IIT (BHU) Varanasi for his exceptional supervision, expert guidance, stimulating discussions, unwavering support, and invaluable assistance throughout my research work. The supportive nature and effective guidance of my mentor fostered a positive research environment that greatly contributed to enhancing my technical writing and presentation abilities, in addition to successfully achieving our research goals.

I express my sincere gratitude to **Prof. M.K.Mondal** of the Department of Chemical Engineering and Technology, **Dr. Sanjeev Kumar Mahto** from the School of Biomedical Engineering at IIT BHU, and **Dr. Ashutosh Dubey** from the Department of Ceramic Engineering at IIT BHU, for their invaluable contribution as members of my research progress evaluation committee. Their insightful feedback, motivation, and unwavering support during my doctoral studies have been instrumental in helping me achieve my thesis objectives.

I owe my personal thanks to **Prof. M.K.Mondal (Head)**, Department of Chemical Engineering & Technology, IIT (BHU) for encouraging and providing me all the facilities to carry out my research work.

I would like to express my sincere thanks to all DPGC members for their direct or indirect motivation and assistance from different corners during my research work at institute. Also, I express my sincere thanks to all faculty members and non-teaching staff of the Department of Chemical Engineering and Technology, Indian Institute of Technology (BHU) for their continued help and co-operation for the completion of this dissertation work.

I am grateful to **Dr. Ashish N. Sawarkar** from the Department of Chemical Engineering at MNNIT Prayagraj for his unparalleled motivation and support throughout my entire PhD program.

I am grateful to my senior, **Dr. Kaushal Kumar Mahto**, for providing me with sincere guidance,

cooperation, and motivation throughout my entire thesis work. I am also thankful to all my lab-mates, namely **Mr. Sudhir Ranjan, Mr. Kedar Sahoo, Ms. Prachi Srivastava, Mr. Vivek Kumar Verma, Ms. Rinki Verma, Mr. Prarabdh Jain, Mr. Alok Kumar, and Mr. Anshuman Singh** for their valuable help and moral support throughout this journey.

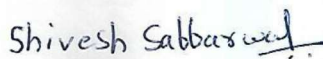
I would like to express my deepest and heartfelt thanks to my friends **Dr. Ravi Sonwani, Dr. Diwakar Pandey, Dr. Ahmad Nawaz, and Dr. Mohit Kumar**. They are always been a source of inspiration for me and stood by my side at the toughest times.

I acknowledge the Ministry of Human Resource Development (MHRD), New Delhi, India for their time to time financial support during my stay at IIT (BHU). I am also grateful to the Department of Science & Technology under the Ministry of Science & Technology of the Government of India for providing financial aid for fueling the research. I am also thankful to the Indian Institute of Technology (BHU) Varanasi, India, for providing the laboratory as well as research facility during my Ph.D. tenure.

Finally, I express my deepest gratitude to my parents, **Mr. Satish Kumar Sabbarwal and Mrs. Maya Sabbarwal**, as well as to my beloved wife, **Kratika Sabbarwal**, and our precious newborn daughter, **Keesha Sabbarwal**. Their unwavering support, encouragement, and motivation have been a constant source of strength for me throughout my academic journey, including the successful completion of my Ph.D. I am truly thankful for their invaluable contributions to my life and career.

Date: 28.6.2023

Place: IIT (BHU), Varanasi


(Shivesh Sabbarwal)

Contents

	Certificate	iii
	Declaration by the Candidate	iv
	Copyright Transfer Certificate	v
	Acknowledgments	vi-vii
	List of Figures	xiii-xvii
	List of Tables	xviii-xix
	List of Abbreviations and Symbols	xx
	Preface and Thesis Organization	xxi-xxvi
Chapter-1	Introduction	1-28
	1.1 Introduction	1
	1.2 Brief Summary of Cancer Disease	1
	1.2.1 Computed tomography imaging	4
	1.2.2 Magnetic Resonance Imaging	5
	1.2.3 Single-Photon Emission Computed Tomography (SPECT)	6
	1.2.4 Fluorescence Imaging	6
	1.3 Main Techniques for Cancer Treatment	8
	1.4 Photothermal therapy's significance in cancer treatment	11
	1.5 The Significance of Fluorescent nanoclusters and Metal nanoparticles in Optical Imaging and Photothermal Therapy	13
	1.6 Synthesis methods required for fluorescent metal nanoclusters	14
	1.6.1 Chemical based synthesis routes	15
	1.6.2 Hydrothermal method synthesis	17
	1.6.3 Microwave based synthesis	18

	1.6.4 Biomineralization mediated Synthesis	18
	1.6.5 Sonochemical assisted synthesis	20
	1.6.6 Photoreduction method	20
	1.6.7 Chemical etching-based synthesis	20
	1.7 Problem Statement defined	23
Chapter- 2	Review of Literature	29-53
	2. Review of Literature	29
	2.1 Development of Metallic Quantum Nanoclusters	29
	2.2 Physical Properties for metallic fluorescent clusters	34
	2.2.1 Optical absorption	34
	2.2.2 Photoluminescence Property	35
	2.2.3 Ultrafast dynamics of metal clusters	37
	2.2.4 Chirality Properties	38
	2.3 Development of alkaline earth metal based nanoclusters	39
	2.4 Nucleation Rate and Interfacial Energy Analysis of CaCO ₃ nanomaterials on various substrates and additional approaches to measure nucleation rate of other nanosystems	43
	2.5 Use of Model free methods for computation of activation energy of nucleation	46
	2.6 Development of various methods for synthesis of tin nanocrystals	48
	2.7 Problem Statement	50
	2.8 Aim and objectives of present work	51
Chapter- 3	Synthesis of biocompatible, BSA capped fluorescent CaCO₃ pre-nucleation nanoclusters for cell imaging applications	55-111
	3.1 Introduction	55
	3.2 Experimental Section	60
	3.2.1 Synthesis of FCPN	60
	3.2.2 Cell Culture and FCPN Treatment	61
	3.2.3 MTT Assay	62
	3.3 MALDI-MS	62

	3.4 Lifetime	63
	3.5 Fluorescence Microscopy	63
	3.5.1 Corrected total cell fluorescence (CTCF) analysis	63
	3.5.2 Quantum Yield	63
	3.5.3 Quantitative methodology for determination of Nanocluster Concentration	65
	3.6 Results and Discussion	67
	3.7 Characterization	67
	3.7.1 Transmission Electron Microscopy (TEM) and XRD Analyses	67
	3.7.2 XPS analysis of FCPN	70
	3.7.3 Fluorescence Characterization of FCPN	77
	3.7.4 UV-Visible spectroscopic studies	79
	3.7.5 MALDI-MS measurements	80
	3.7.6 Fluorescence Lifetime Analysis of FCPN	82
	3.7.7 FTIR analysis of FCPN	87
	3.8 Design Rational of FCPN	88
	3.9 Optimization of Synthesis Procedure for FCPN	93
	3.10 Application of FCPN	94
	3.10.1 FCPN Photostability	94
	3.10.2 MTT Assay	94
	3.10.3 Fluorescence Microscopy	95
	3.10.4 CTCF Analysis & Effect of Cluster Size	96
Chapter- 4	A New Technique for Calculating Kinetic and Thermodynamic Barriers for Nucleation Rates and Interfacial Energy of CaCO₃ Prenucleation Nanoclusters at High Temperature Using TGA Models and In-Situ Crystallization	113-155
	4. Introduction	113
	4.1 COMPUTATIONS	119
	4.2 Computation of apparent activation energy of CCPN for random nucleation	120
	4.3 Computation of pre-exponential kinetic factor (A_{α}) of CCPN	125
	4.4 Calculating the CCPN's thermodynamic barriers, which are necessary for the start of random	126

	nucleation	
	4.5 Nucleation rate calculation using kinetic and thermodynamic barriers and interfacial energy calculation using thermodynamic barriers	127
	4.6 Experimental Section	128
	4.6.1 Synthesis of CCPN	128
	4.7 Results and Discussion	128
	4.7.1 Physico-Chemical Characterization and Studies	129
	4.7.2 Reaction Kinetics and corresponding Pathways	135
	4.7.3 Analysis of apparent activation energy in opposition to reaction progression	137
	4.7.4 Computation of pre-exponential kinetic factor as a function of conversion	141
	4.7.5 Computation of Thermodynamic parameters against the reaction progression	142
	4.7.6 Variation of nucleation rate with extent of conversion and Temperature	145
	4.7.7 Variation of Interfacial Energy with Temperature and Reaction Progression	147
Chapter- 5	Room-Temperature Stabilized α-Sn nanocrystals for <i>in-vivo</i> Toxicology Evaluation and Photothermal Therapy Corroborated by FFT-Modeling	157-196
	5.1 Introduction	157
	5.2 Materials and Methods	161
	5.2.1 Equipment and Materials	161
	5.2.2 Materials used for <i>in-vitro</i> photothermal application:	162
	5.3 Methods	162
	5.3.1 Hypothesis	162
	5.3.2 Animals	163
	5.3.3 <i>In-vivo</i> acute toxicity study:	164
	5.3.4 Organ coefficient	164
	5.3.5 Biochemical analysis	165
	5.3.6 Statistical analysis	165
	5.4 Methods used for <i>in-vitro</i> photothermal application:	165

	5.4.1 Cell line maintenance:	165
	5.4.2 Pre-Photothermal and Post-Photothermal in-vitro cell culture procedure:	166
	5.4.3 Bright field image:	166
	5.4.4 FFT weighted Bright field imaging:	167
	5.5 Photothermal efficiency calculation steps for tin nanocrystals:	169
	5.6 Results and Discussion	170
	5.6.1 Room temperature synthesis of alpha tin nanocrystals with beta phase, as explained through XRD, HR-TEM, and SAED characterizations	170
	5.6.2 Inductively coupled plasma mass spectrometry (ICP-MS) analysis and photothermal characterization	176
	5.6.3 Fast Fourier Transform (FFT) weighted Bright Field Imaging	181
	5.6.4 The predicted model pre-photothermal operation acquainted by FFT approach:	184
	5.6.5 Biocompatibility assessment of tin nanocrystals within the Wistar Rats	187
	5.6.6 Weight fluctuation in Wistar RATS during tail vein administration of tin nanocrystals:	190
	5.6.7 Organ Coefficient in Wistar RATS during tail vein administration of tin nanocrystals:	190
	5.6.8 Biocompatibility assessment on intravenously injected tin nanocrystals through histopathological and blood serum enzyme assessments	191
Chapter -6	6. Conclusions and Future Work	197-203
	6.1 Conclusions	197
	6.2 Future Scope	201
	References	205-229
	List of Publications	231-232

List of Figures

Figure No.	Title	Page
Chapter 1		
1.1	Distinction between Normal Cells and Cancerous Cells in terms of Controlled and Uncontrolled Growth.	2
1.2	Various synthesis methods for metallic clusters used in the fields of bioimaging and cancer treatment.	4
1.3	Illustration of Diverse Approaches Utilized in Cancer Treatment.	9
1.4	The differentiation between bulk material, powdered material nanoparticles, nanoclusters, and atoms, highlighting two distinct processes known as Top-down synthesis and Bottom-up synthesis.	15
1.5	Increasing the biomineralization agent concentration confines the metal clusters tightly	19
Chapter 3		
3.1	TEM image of large size CaCO ₃ Nanoparticles (NP'S) ~49 nm (Control A) synthesized (without BSA), using leaf extract of Moringa oleifera as reducing agent.	61
3.2	Fluorescence Spectra of FCPN against Rhodamine 6G for calculation of Quantum Yield of FCPN (green emission).	65
3.3	The FCPN (a) Size distribution and TEM image (b) XPS Spectra. (c) MALDI-MS spectra. (d) Comparative fluorescence lifetime (model fitted) for red, green and blue emission of FCPN.	68
3.4	XRD analysis of FCPN	70
3.5	XPS spectra: M.oleifera leaf extract (a) O1s, peak at 533 eV (b) Ca2p _{3/2} and Ca2p _{1/2} of free Ca ²⁺ in M.oleifera leaf extract, peak at 347.6 eV and 350.9 eV. XPS spectra: FCPN (c) C1s of C-C, peak at 284.6 eV. (b) C1s of CO ₃ ²⁻ , peak at 287.3 eV.	72
3.6	(a) XPS spectra (O1s) FCPN. (b) Time dependent viability of MG-63 cells against FCPN treatment. *indicates the statistical significant difference among the samples with respect to control, cultured for 3 days, **indicates the statistical significant difference among the samples with respect to their respective control sample (culture media), and ***indicates the significant difference among the samples, incubated for 5 and 7 days with respect to those of 3 days (P<0.05)./experiment repeated 3 times (c) Images of FCPN (1) Ex./Em 366 nm/Bluish white ,(2) Ex./Em. 595 nm /Red (3) (Ex./Em. 472 nm/ Green (4) Ex./Em. 516 nm/Yellow) (5) Under sun light exposure. (d) Photostability of FCPN.	73

3.7	Reaction scheme	75
3.8	Fluorescence Spectra-FCPN: (a)-(Absorbance, C1) = 366 nm, λ_{exc} = 366 nm, λ_{em} = 476 nm-blue). (b)-(Absorbance, C2 = 472 nm, λ_{exc} = 472 nm, λ_{em} = 541 nm-green). (c)-(Absorbance, C3 = 516 nm, λ_{exc} = 516 nm, λ_{em} = 595 nm-yellow). (d)-(Absorbance, C4 = 560 nm, λ_{exc} = 560 nm, λ_{em} = 636 nm-red).	76
3.9	3D Fluorescence spectra: (a) FCPN (leaf extract) (b) Control C (pure ascorbic acid) (c) Comparative fluorescence intensity of FCPN, Control A, Control B and Control C at different excitations (Ex.) and emissions (Em.)..	78
3.10	Absorption spectra: FCPN and BSA in the range from 279 to 293 nm.	79
3.11	FCPN, BSA and Moringa leaf extract in the range from 279 to 281 nm. (b) FCPN, BSA and Moringa leaf extract in the range from 291 to 293 nm.	80
3.12	MALDI-MS spectra of (a) BSA, and (b) Moringa leaf Extract.	81
3.13	Fluorescence lifetime (FL) spectra of (a) FCPN (b) BSA Protein (c) leaf extract, with ex/em 375/485 nm; FL spectra of (d) FCPN (e) BSA protein (f) leaf extract with ex/em of 496/565 nm, using LED lamp as excitation source; FL Spectra of (g) FCPN (h) BSA Protein (i) leaf extract, with ex/em of 598/674 nm, using LED lamp as excitation source; All of the above images contains inset figure showing the zoomed images of the same curve.	84-85
3.14	Band energy gap for FCPN.	86
3.15	Fluorescence spectra of FCPN under different excitations (ex.) and different emissions (em.).	87
3.16	FTIR spectra: (a) FCPN and BSA, (b) zoomed image of FCPN and BSA in the range varying from 2300 cm ⁻¹ to 2400 cm ⁻¹ .	90
3.17	XPS spectra: large size CaCO ₃ Nanoparticles (NP'S) ~49 nm (Control A). (a) Ca _{2p} 3/2 of Ca ²⁺ , peak at 347.6 eV. (b) Ca _{2p} 1/2 of pure calcite crystal, peak at 351.2 eV.	91
3.18	Fluorescence stability of FCPN over a period of time (4 months) at: (a) Ex. 366 nm, Em. 477 nm, (b) Ex. 472 nm, Em. 541 nm, (c) Ex. 516, Em. 595 nm (d) Ex. 560 nm, Em. 636 nm.	92
3.19	pH stability of FCPN at different pH, ranging from 5.8 to 12.	93
3.20	<i>In-vitro</i> multicolor fluorescent images of MG-63 cells incubated with FCPN (a) Ex./Em: 472/541 nm. (b) Ex./Em: 366 /477 nm. (c) Ex./Em: 516/595 nm. (d) Ex./Em: 472/ 636 nm. (e) merged. (f) bright field images.	100

3.21	Z stack confocal images of MG-63 cell incubated with FCPN (Ex.366 nm, Em. Blue). (a)= 0 μm . (b) = 2 μm . (c) = 4 μm . (d) = 6 μm . (e) =8 μm . (f) = 10 μm . (g) = 12 μm . (h) = 14 μm . (i) = 16 μm .(j) = 18 μm . (k) = 20 μm . (l) = 22 μm . (m) = control (culture media).	102
3.22	Z stack confocal images of MG-63 cell incubated with FCPN (Ex. 472 nm, Em. Green). (a)= 0 μm . (b) = 2 μm . (c) = 4 μm . (d) = 6 μm . (e) =8 μm . (f) = 10 μm . (g) = 12 μm . (h) = 14 μm . (i) = 16 μm .(j) = 18 μm . (k) = 20 μm . (l) = 22 μm . (m) = control (culture media).	103
3.23	Z stack confocal images of MG-63 cell incubated with FCPN (Ex.472 nm, Em. Red) (a)= 0 μm . (b) = 2 μm . (c) = 4 μm . (d) = 6 μm . (e) =8 μm . (f) = 10 μm . (g) = 12 μm . (h) = 14 μm . (i) = 16 μm .(j) = 18 μm . (k) = 20 μm . (l) = 22 μm . (m) = control (culture media).	104
3.24	Fluorescent microscopy images of MG-63 cells incubated with culture media (control) (a) (Ex. 472 nm), (b) (Ex. 366 nm), (c) (Ex. 516) (d) (Ex. 472 nm).The control images appear to be dark, due to lack of emission from the samples.	105
3.25	Mean Luminescence Intensity in MG-63 cells (1) FCPN [Ex. 366 nm, Em. Blue (477 nm)] (2) FCPN [Ex. 472 nm, Em. Green (541 nm)] (3) FCPN [Ex. 472 nm, Em. Red (636 nm)]: (a) = 0 μm , (b) = 2 μm , (c) = 4 μm , (d) = 6 μm , (e) = 8 μm , (f) = 10 μm , (g) = 12 μm , (h) = 14 μm , (i) = 16 μm , (j) = 18 μm , (k) = 20 μm , (l) = 22 μm .	106-107
Chapter 4		
4.1	(a) Detailed histogram for CCPN clusters acquired by TEM (b) TEM image of CCPN clusters at 20 nm magnification (c) Ultrasmall CCPN clusters (0.5-1 nm)	129
4.2	TEM images of CaCO ₃ Prenucleation clusters at different magnifications	130
4.3	(a) XRD of CaCO ₃ Pre-nucleation cluster (b) XRD of Calcite/CaS formed after nucleation of CaCO ₃ Pre-nucleation clusters at 500 °C.	131
4.4	(a) Mechanism of Carbonate ion synthesis.	133
4.5	(a) XPS analysis for ultra-small CCPN clusters (b) FTIR analyses for CCPN and BSA protein from 500 to 4500 cm ⁻¹ (c) Absorbance of aqueous solution for CCPN and BSA protein together.	134
4.6	(a) Comparison of experimental and theoretical values (Product of integral and differential function) at different heating rates 10, 15 and 20 °C/min by acquiring Z(α) master plots, CCPN (b) Variation of apparent activation energy (E_a) with conversion (α), as predicted by different iso-conversional techniques, CCPN (c) The plot of iterative iso-conversional method for computation of apparent activation energy (E_a) from the slope of Straight lines at respective conversions.	140
4.7	(a) TGA, DTG curve of CCPN at heating rate of 10 °C/min (b) TGA, DTG curve of CCPN at heating rate of 15 °C/min (c) TGA and DTG curve of CCPN at heating rate of 20 °C/min (d) Comparison of DTG Curves of CCPN at different heating rates 10,15, and 20 °C/min.	143
4.8	(a) The curve for pre-exponential kinetic factor (A_0) with reaction progression having units units S^{-1} and nuclei $\mu\text{m}^{-2}\text{min}^{-1}$ at different heating rates 10, 15, and 20 °C/min, CCPN (b) The curve for Change in enthalpy (ΔH) with Conversion at different heating rates 10, 15, and 20 °C/min, CCPN (c) The curve for Change in Gibbs Free energy (ΔG) with Conversion at different heating rates 10, 15, and 20 °C/min, CCPN (d) The curve for Change in entropy (ΔS) with Conversion at different heating rates 10, 15, and 20 °C/min, CCPN.	145

4.9	(a) Nucleation Rates curve for CCPN with temperature at heating rate of 10, 15 and 20 °C/min (b) Logarithm of Nucleation Rate Curve with reciprocal of temperature for CCPN at heating rate of 10, 15 and 20 °C/min (c) Nucleation Rates curve for CCPN with reaction progression at heating rate of 10, 15 and 20 °C/min.	149
4.10	(a) Interfacial energy curve of CCPN with temperature at heating rate of 10, 15 and 20 °C/min (Linear Fit) (b) Interfacial Energy curve of CCPN with conversion at heating rate of 10, 15 and 20 °C/min (Polynomial FIT).	150
Chapter 5		
5.1	(A) The experimental XRD pattern was compared to crystallographic open database (COD) files to confirm α -Sn formation with β -Sn and to rule out existence of pure alternative phases, such as SnO ₂ and SnO. (B) TEM analysis of ultra-small Sn nanocrystals with an average diameter of 4.90 nm and a standard deviation of 2.30 nm. (C) Using FFT (Fast Fourier Transform), d-spacing values are estimated at 0.336 nm and 0.29 nm, respectively, for β -Sn (111) and β -Sn (020) crystals. (D) FFT (Fast Fourier Transform) estimates d-spacing at 0.374 nm for α -Sn (111) crystals. (E) FFT (Fast Fourier Transform) estimates d-spacing at 0.372 nm for α -Sn (111) crystals. (F) FFT (Fast Fourier Transform) estimates d-spacing at 0.337 nm for β -Sn (111) crystals. (G) Tin nanocrystal formation as revealed by the selective area electron diffraction pattern (SAED). (H) Another selective area electron diffraction pattern (SAED) revealed the formation of tin nanocrystals.	173
5.2	Sn cubic α -Sn (111) peak with a d-spacing of 0.384 nm was found in the XRD spectra of Sn nanocrystals (SSN), detected by Match software.	174
5.3	Sn tetragonal β -Sn (020) and β -Sn (011) peaks with d-spacing of 0.291 and 0.279 nm was found in the XRD spectra of Sn nanocrystals (SSN), detected by Match software.	175
5.4	No pure SnO ₂ and SnO phase peaks were detected by the XRD spectra of Sn nanocrystals (SSN) using Match software.	176
5.5	(A-B) Calibration standard preparation before acquiring Sn concentration by ICPMS. (C) The measured concentration of synthesized Sn nanocrystals (790.8 ppm) in deionized water by ICPMS. (D) The value of the absorbance (A ₁) at high concentration of tin nanocrystal (Q ₂ = 1.0544 mg/ml) is higher when compared to the absorbance value (A ₂) at the low concentration of tin nanocrystal (Q ₁ =0.7908 mg/ml) at the specific 980 nm wavelength.	179
5.6	(A) Synthesized tin nanocrystals in water as aqueous solution. (B) Direct band gap of tin nanocrystals is estimated to be 2.38 eV, close to alpha tin nanocrystals (2.2 eV). (C) The absorbance spectra of tin nanocrystals over a wide wavelength range between 200 nm and 1100 nm. (D) Temperature vs time spectra for tin nanocrystals at concentration of 1.5816 mg/ml and corresponding efficiency calculation by $-\ln(\theta)$ vs time plot (E) Time-dependent temperature rise in an aqueous solution of 1.5816 mg/ml tin nanocrystals, compared to water as a control subjected to irradiation at several laser power densities (0.83, 1.18 and 1.69 W/cm ²). (F) The time-dependent temperature rise in tin nanocrystal aqueous dispersion when concentration was increased from 0.7908 to 1.58 mg/ml. (G) The increase in photothermal temperature is continuous after synthesis and over the next seven days. (H) A remarkable photothermal stability at 980 nm laser wavelength over 180 minutes of heating and cooling cycles. (I) Tin nanocrystals at various concentrations was subjected to an MTT test after and before being exposed to a 980 nm laser. (J) Bright-field image shows cells with 110 μ g/ml tin nanocrystals, as well as the morphology of cells both before and after being irradiated by a 980 nm laser.	180

5.7	(A-B) Bright-field image: The morphology of cells before irradiation by laser with varying tin nanocrystal concentrations, with 110 µg/ml and 50 µg/ml tin nanocrystals, respectively, and 1, 2, and 3 pointed cells selected for FFT analysis. (C-D) The morphology of cells after being irradiated by a 980 nm laser, and 1', 2', and 3' pointed cells selected for FFT analysis. (E) The morphology of control cells carrying culture media with 1'' pointed cell was chosen for FFT imaging analysis,	181
5.8	(A) FFT Spectrogram for selected control cell (B) 2D signals generated through IFFT for control cell (C) G-C(x) is one dimensional amplitude modulated wave signal generated through 2D IFFT signal in x domain for the control cell. (D) Enveloped wave signal generated through amplitude modulated wave signal (E) Amplitude vs Frequency signal generated through FFT of amplitude modulated wave (F-H) 2D signals generated through IFFT of selected cell (1,2, and 3 pointed morphology) carrying Sn NCs (110 µg/ml).	182
5.9	Fast Fourier Transform weighted single cell Bright-field imaging: Pre-Photothermal (A) FFTG-2D FFT Spectrum in green channel on 3 selected cells with 110 µg/ml Sn NC. (B) FFTS-2D FFT spectrogram carrying 110 µg/ml Sn NC on three individual cells (C) IFFT extracted amplitude modulated wave signal G-1(x), G-2(x) & G-3(x) under x domain. (D) Extraction of envelope wave signal from amplitude modulated wave (E) Amplitude vs frequency signal extracted from envelope wave signal. Post-Photothermal: (F) FFTG-2D FFT Spectrum in green channel on 3 selected cells with 110 µg/ml Sn NCs. (G) FFTS-2D FFT spectrogram carrying 110 µg/ml Sn NCs on three individual cells. (H) G-1(x), G-2(x) & G-3(x) signals diminishes after photothermal treatment. (I-J) FFTS-2D FFT spectrogram carrying 50 µg/ml Sn NC on three individual cells before and after photothermal.	186
5.10	(A-E) Typical photographs that exhibit the normal morphology of Heart, Kidneys, Lungs, Spleen, Liver treated rats after single-dose intravenous administration of Sn nanocrystals at concentrations of $Q_1=0.7908$ mg/ml, $Q_2=1.0544$ and $Q_3= 1.5816$ mg/ml. (F-J) Effect of single dose intravenous administration of Sn nanocrystals at concentrations of $Q_1=0.7908$ mg/ml, $Q_2=1.0544$ and $Q_3= 1.5816$ mg/ml on highly perfused organs like Heart, Kidneys, Lungs, Spleen, Liver , stained with eosin and hematoxylin, showcasing the intricate structures within. (K-L) Effect of single dose intravenous administration of different concentrations of tin nanocrystals on body weight and average food consumption at various intervals during 14 days of the experimental protocol. All values are displayed as mean±SD (n=6 male rat/group). (A statistical analysis method consisting of a two-way analysis of variance, followed by Bonferroni post hoc test).	189
5.11	(A-E) Effect of single dose intravenous administration of Sn nanocrystals on organ coefficient of Heart, Kidneys, Lungs, Spleen, Liver after end of experimental protocol. All values are displayed as mean±SD (n=6 male rat/group). (One-way ANOVA, followed by Turkey's multiple comparison post hoc test). (F-J) Effect of single dose intravenous administration of Sn nanocrystals on serum concentration of Heart, Kidneys, Liver, Lungs, after end of experimental protocol. All values are displayed as mean±SD (n=6 male rat/group). (One-way ANOVA, followed by Turkey's multiple comparison post hoc test).	193

List of Tables

Table No.	Title	Page
Chapter 3		
1	Fluorescence lifetime of FCPN, BSA and leaf extract	82
2	Comparison table for biocompatibility, spectroscopic, physical, chemical and other properties for FCPN, Alexa Fluor organic dye, gold fluorescent cluster and magnesium fluorescent cluster.	109-111
Chapter 4		
1	Reaction Pathways for solid state reaction in terms of models governed by Integral function and Differential function.	137
2	The values of apparent activation energy (E_{α}) computed by different iso-conversional methods.	139
3	Pre-exponential Kinetic factor A_{α} computed by differential function $f(\alpha)$ of Random Nucleation within CCPN matrix.	141
4	Thermodynamic parameters required for CCPN nucleation at different heating rates and respective conversion.	142
5	Nucleation Rate computed by Kinetic and Thermodynamic barriers required for Random Nucleation within CCPN matrix with Temperature.	150
6	Interfacial energy computed by Thermodynamic barriers within the CCPN matrix with Temperature.	151
Chapter 5		
1'	Comparison study of Sn nanocrystals with other systems.	159
1''	Photothermal efficiency of tin nanocrystals (current study) with prior studies.	161
1	The measured values of 'lattice fringes' calculated by Selective area electron diffraction pattern (SAED), High resolution transmission electron microscopy (HRTEM), and High Resolution X-ray diffraction (HR-XRD) analyses. The data for predicted values of lattice fringes were obtained through Crystallography Open Database (COD), COD-1512542, with American Mineralogist Crystal Structure Database (AMCSD), AMCSD-0011246 for α -Sn, and COD-7222460 with AMCSD-0012875 for β -Sn.	172
2	Containing fitted sine wave parameters for control and selected cells, carrying Sn NCs (110 $\mu\text{g/ml}$), Pre-photothermal.	184
3	General behavioral and observation analysis for the first 4 hrs. and during 14 days after single-dose administration of different concentrations of tin nanocrystals ($Q_1=0.7908$ mg/ml, $Q_2= 1.0544$	188

	and Q3= 1.5816 mg/ml) in rats (n = 6 male rats/group).	
--	--	--

List of Abbreviations and Symbols

Abbreviation	Nomenclature
CTI	Computed tomography imaging
MRI	Magnetic resonance Imaging
SPECT	Single-Photon Emission Computed Tomography
BI	Bioluminescence imaging
FI	Fluorescence imaging
PTT	Photothermal therapy
NIR	Near-infrared light
FCPN	Fluorescent calcium carbonate prenucleation clusters
Qd's	Quantum dots
BSA	Bovine Serum Albumin
MTT Assay	3-(4, 5-dimethylthiazol-2-yl)-2, 5-diphenyl tetrazolium bromide
CTCF	Corrected total cell fluorescence (CTCF) analysis
TGA	Thermogravimetric analysis
CCPN	Calcium carbonate prenucleation clusters
m_0	Initial weight of CCPN before TGA
m_f	Final weight of CCPN after TGA
α	Conversion
J_0	Kinetic barrier of nucleation
A_α	Pre-exponential kinetic factor
E_α	Activation energy of nucleation
R	Gas constant
ΔG	Change in Gibbs free energy
ΔH	Change in enthalpy
ΔS	Change in entropy
$exp(\Delta G/RT)$	Thermodynamic barrier
I	Nucleation Rate
$f(\alpha)$	Differential function
$g(\alpha)$	Integral function
β	Heating Rate
vyazovkin AIC	Vyazovkin Advanced isoconversional method
T_p	Peak temperature in DTG curve
K_B	Boltzmann constant
h	Plank constant
σ	Interfacial energy of nanomaterial
ρ_{nm}, M, v_0, N_A	Density, molar mass, specific volume, Avogadro Number
$z(\alpha)$	Product of differential and integral function
FFT	Fast fourier transform
IFFT	Inverse Fast fourier transform

Preface and Thesis Organization

Nanomaterials are gaining compelling interest among various scientific communities owing to their vast applications in the area of energy, health and environment. Over the decades, ample amount of work has been done on nanomaterials due to their unique opto-electronic properties when compared to the bulk materials. Among various nanomaterials investigated, noble metals such as Au, Ag and Cu are most popular fluorescent material owing to their several unique properties like fluorescence, near infrared absorption, catalytic capability, and enzymatic settings. In recent years, the research is turning out to create more biocompatible materials owing to existence of long-term toxicity during *in-vivo* study on noble metals. Herein, an attempt to synthesize fluorescent biocompatible nanomaterials based on alkaline earth metal has been taken up, to harness their multicolor emission. To synthesize such type of ultra-small clusters, a low cost protein Bovine Serum Albumin (BSA) is utilized and leaf extract is used as a reducing agent. Such type of synthesis uses BSA protein and leaf extract can be abbreviated as bio-mineralization based synthesis, and these clusters in the current study are basically used as a bio imaging agent. The synthesized fluorescent nano clusters (CaCO_3) demonstrate an average size of around 1.3 nm, exhibiting fluorescence lifetimes that range from 1.05 ns to 30.60 ns. These clusters contain varying numbers of atoms, ranging from 16 to 936 molecules. Additionally, their penetration depths, ranging from 4 μm to 6 μm , are attributed to their diverse sizes, highlighting their adaptability for a wide range of applications. Additionally, the research highlights the biocompatibility of these clusters, as indicated by an observed increase in cell viability over a 7-day incubation period. On the contrary, understanding nucleation kinetics of ultra-small clusters at high temperatures provides critical insights into the thermodynamic behavior of the system, including the activation energy required for nucleation. This knowledge is instrumental in designing efficient

synthesis routes and predicting the stability of resulting clusters across varying conditions. Moreover, this understanding allows researchers to tailor the synthesis process to optimize cluster properties for specific applications, enhancing their performance and functionality in catalysis, optics, and biomedical fields. Hence, the next research was focused towards the calculation of nucleation rate of ultra-small clusters in high temperature range (100 °C- 600 °C). But there was no engineered technology to calculate the same mathematically. To address this issue, I employed thermogravimetric (TGA) analyses to assess the nucleation rate of ultra-small clusters across a high-temperature range (100 °C- 600 °C) and varying conversion levels (0.1-0.9). Through this method, numerical parameters such as the activation energy (128.041 kJ mol⁻¹) with a systematic error of ≤ 0.005 , and the pre-exponential kinetic factor (1020–1030 min⁻¹) were determined. Additionally, nucleation rates corresponding to different temperature increments were elucidated: at 10 °C min⁻¹: 22,337, 15 °C min⁻¹: 33,636 min⁻¹, and 20 °C min⁻¹: 88,140. The interfacial energy with temperature was also analyzed, revealing values of 66.77 mJm⁻² at 10 °C min⁻¹, 67.39 mJm⁻² at 15 °C min⁻¹, and 68.05 mJm⁻² at 20 °C min⁻¹. The temperature required for crystallization (500 °C) was highlighted, providing crucial insights into the synthesis process and the thermodynamic behavior of the clusters. Moreover, the development of a bioimaging agent for diagnosing diseases such as cancer is a crucial step in early detection and treatment planning. The clusters being within the 10 nm barrier of kidney filtration limit and the constituent elements present in the cluster are among one of the elements already present in the body, its metabolism will only lead to formation of harmless by products such as CO₂ and calcium, which underscores their biocompatibility and safety for medical use. However, for the treatment of cancerous tissues, a different approach is required. Thus, tin (Sn) nanoparticles have been selected for their biocompatibility, small size (less than 10 nm),

and high photothermal efficiency (42.4%). Hence these nanoparticles hold promise for targeted cancer therapy, delivering localized heat to cancer cells while minimizing damage to healthy tissues. This dual approach, employing bioimaging agents for diagnosis and therapeutic nanoparticles for treatment, highlights the multifaceted nature of nanotechnology in healthcare, offering innovative solutions for combating diseases like cancer. But synthesis of alpha tin nanoparticles at room temperature were understood challenging owing to their instability under ambient conditions. Many scientific groups synthesized alpha tin nanoparticles with the help of large sized substrates (>70 nm) like CdTe, InSb and silicon with matching lattice constant and used high temperature for the synthesis. To address this issue, we successfully synthesized alpha tin nanocrystals in solvent water at ambient temperature without utilizing any bulky substrates by tuning their direct band gaps. Hence, the current synthesis includes the synthesis of substrate free tin nanocrystals and their biomedical applications. With a photothermal efficiency of 42.4%, it efficiently converts light into heat for therapeutic use. Stable at room temperature, it ensures practicality in various settings. Its strong absorption in the NIR region (800-1100 nm) indicates its suitability for targeted therapies. *In-vivo* studies on Wister rats report no adverse effects on vital organs, affirming its safety. The absence of poisonous substances in synthesis underscores its biocompatibility. With a promising potential for cancer treatment, it demonstrates efficacy under low-power NIR light ($0.83\text{W}/\text{cm}^2$). Cellular response prediction is facilitated by FFT-weighted images on a scale from 0 to 100, allowing precise evaluation. With ultra-small, free-standing tin nanocrystals arranged in a diamond-cubic structure, measuring just 4.9 nm, this material exhibits highly desirable physical properties. Synthesized in aqueous phase using deionized water, it offers versatility and compatibility with biological systems. Hence,

this thesis is mainly consisting of six chapters followed by references and publications list. A brief introduction about separate chapters is demonstrated below;

Chapter 1 includes the detailed investigation about the requirement of biocompatible nanoclusters, and a brief description about pros and cons of various cancer diagnostic and treatment tools. The various new methods for metallic cluster synthesis such as chemical, hydrothermal, biomineralization, microwave, sonochemical, photochemical, and chemical etching routes are discussed in current chapter. The reason of selection of biomineralization synthesis method was also discussed in the current chapter. In spite of above, reason of selection of optical fluorescence imaging and photothermal therapy is also discussed in detail. Ultimately a brief paragraph on problem statement is defined.

Chapter 2 includes development of metallic fluorescent clusters and their properties, followed by the development of many synthesis techniques for fabricating nano systems based on Ca and Mg. The luminescent properties of various CaS phosphors were investigated and their flaws are also provided in the literature survey. More over development of fluorescent magnesium clusters were also mentioned in the literature review. On the other hand, hurdles to the calculation of nucleation rate and interfacial energy at high temperature and respective conversions are also addressed. Tin nanoparticles development are also discussed in the literature survey. Problem statement and objective of the thesis are also discussed.

Chapter 3 provides the synthesis of fluorescent CaCO_3 prenucleation clusters with high cellular uptake, low toxicity, eminent photostability, astonishing biocompatibility, excellent water dispersibility, and low cost of synthesis. Besides, such CaCO_3 material can easily get decomposed inside the body producing CO_2 and water as decomposition products. Besides high reactivity of magnesium and calcium, the synthesis of fluorescent BSA protected magnesium clusters (Mg-S) opens a new avenue for synthesis of BSA

capped CaCO_3 prenucleation nanoclusters (FCPN). To perform such synthesis, *M. oleifera* leaf extract is used as reducing agent. To restrict the size of the CaCO_3 , non-toxic, low cost and readily available, BSA protein was used as a capping and stabilizing agent.

Chapter 4 discusses computation of J_0 (kinetic energy barrier) at high temperature and respective conversion for BSA capped CaCO_3 prenucleation clusters (CCPN) (1-2nm). A_0 (pre-exponential kinetic factor) for CaCO_3 prenucleation clusters was determined through differential function $f(\alpha)$ linked to random nucleation process. This is the first time that TGA technology was used to calculate the nucleation rates and interfacial energy of such ultra-small nanoclusters at high temperatures and respective conversions followed by start of random nucleation within the matrix of CCPN through distortion of kinetic and thermodynamic boundary. The randomness of third-order nucleation was demonstrated using $z(\alpha)$ master plots. Moreover, thermodynamic parameters such as ΔG , ΔH , and ΔS were computed to estimate thermodynamic barrier required for nucleation to occur. Experimentally the existence of nucleation in CaCO_3 pre-nucleation clusters to Calcite/CaS crystal was performed at the high temperature (500 °C).

Chapter 5 discusses noteworthy global challenge that addresses the synthesis of alpha tin nanocrystals in their substrate-free form along with their beta counterparts, at ambient temperature. The reduction chemistry is utilized to create ultra-small free-standing tin nanocrystals, which are then employed at the interface of engineering and biology, utilizing sophisticated mathematical modeling through FFT, *in-vivo* toxicological assessments in Wistar rats, and *in-vitro* photothermal analyses, which have never been conducted before. The rapid disclosure of the substrate-free tin nanocrystals fabrication process is expected to have extensive implications not only in the realm of biological applications, but also in various other domains, such as superconductivity, the development of layered films similar to graphene materials, lithium-ion batteries and so

on. Thereby, this innovation for synthesizing substrate-free alpha tin nanocrystals in solvent water at ambient temperature marks a significant achievement. These nanocrystals diminutive size, has allowed them to be used for the first time in biological applications. This straightforward, one-pot synthesis technique offers a promising avenue for unlocking their tremendous potential in the impending future.

Chapter 6 discusses the conclusions and future scope for all the developed materials for various biomedical applications and their nucleation rate and interfacial energy analysis at high temperature and respective conversion at high temperature by adopting thermogravimetric (TGA) analysis.